Agricultural and Forest Meteorology 288–289 (2020) 108019

Contents lists available at ScienceDirect

Agricultural and Forest Meteorology

journal homepage: www.elsevier.com/locate/agrformet

Comparison of MODIS-based vegetation indices and methods for winter wheat green-up date detection in Huanghuai region of China

Liqin Gan[a], Xin Cao[a,b,*], Xuehong Chen[a,b], Qi Dong[a], Xihong Cui[a,b], Jin Chen[a,b]

[a] State Key Laboratory of Earth Surface Processes and Resource Ecology, Faculty of Geographical Science, Beijing Normal University, Beijing 100875, China
[b] Beijing Engineering Research Center for Global Land Remote Sensing Products, Institute of Remote Sensing Science and Engineering, Faculty of Geographical Science, Beijing Normal University, Beijing 100875, China

ARTICLE INFO

Keywords:
Winter wheat
Spring green-up date
Vegetation index
MODIS
Phenology detection

ABSTRACT

Satellite vegetation index (VI) time series data provide a feasible option for monitoring crop phenology at a large scale. However, there are limited researches that investigated the accuracy of different methods for crop phenology detection with various VIs over a large-scale region. In this study, we used four VIs, i.e. Normalized Difference Vegetation Index (NDVI), Enhanced Vegetation Index (EVI), Two-band Enhanced Vegetation Index (EVI2), and Normalized Difference Phenology Index (NDPI) derived from the Moderate Resolution Imaging Spectroradiometer (MODIS) data, combined with six methods, i.e. relative threshold at 10%, 20% or 50% of the VI's amplitude (RT10, RT20 and RT50), maxima of the curvature change rate of the fitted logistic curve (CCR_{max}), maxima of the first derivation of the VI curve (β_{max}), and cross-correlogram spectral matching-phenology (CCSM-P), to detect winter wheat green-up dates (GUDs) for the period of 2009–2013 in the Huanghuai winter wheat region of China. The performance of the combinations of these methods and VIs was evaluated using ground-observed GUDs from agrometeorological stations with correlation coefficient (r), regression coefficient (a), root mean square error (RMSE) and bias. We further investigated the spatial trend of residuals from a linear model between satellite- and ground-observed GUDs. Results show that NDPI outperforms the other VIs with the highest consistency with ground data in the whole region. RT10, CCR_{max} and CCSM-P show higher accuracy in the northern region, while in the southern region, RT20 shows relatively higher accuracy in the case of poor performance of all six methods. However, the residuals of these six methods based on NDPI show significantly positive correlations with latitude in the whole region, suggesting an uneven spatial distribution of accuracy with a tendency of underestimating GUDs at the low latitude region and overestimating GUDs at the high latitude region when applying the same method to detect GUDs over a large-scale region. It is suggested to develop a new method or combine several methods to reduce the spatial incoherence of residuals.

1. Introduction

As a key phenological phase, the spring green-up date (GUD), defined as the start time of photosynthetic activity of vegetation, is mainly controlled by climatic factors (Badeck et al., 2004; Khare et al., 2017; Richardson et al., 2006). For agriculture crops, GUD specifically refers to the time when the new leaves begin to grow after the winter growth-break (Zhou et al., 2013). With significant global warming, numerous studies have reported that crop GUD has showed an advancing trend over the past several decades (Estrella et al., 2007; Oteros et al., 2015). Such advance of GUD can not only shape the later growth of crops closely related to crop yield and agricultural practices such as fertilization and irrigation, but also directly or indirectly affect carbon, water cycling and energy balance (Chu et al., 2016). Consequently, accurate monitoring the crop GUD dynamics is urgently needed for agricultural management and better understanding of crop response and adaptation

Abbreviations: β_{max}, maxima of the first derivation of the VI curve; CCR_{max}, maxima of the curvature change rate of the fitted logistic curve; CCSM-P, cross-correlogram spectral matching-phenology; EOS, the end of the season; EVI, Enhanced Vegetation Index; EVI2, Two-band Enhanced Vegetation Index; GUD, green-up date; GGUD-threshold, the percentage threshold of NDPI curve amplitude at the ground GUD point; HHN, Huanghuai North region; HHS, Huanghuai South region; NDPI, Normalized Difference Phenology Index; NDVI, Normalized Difference Vegetation Index; RMSE, root mean square error; RT10, RT20, or RT50, relative threshold at 10%, 20% or 50% of the VI's amplitude; VI, vegetation index

* Corresponding author at: State Key Laboratory of Earth Surface Processes and Resource Ecology, Faculty of Geographical Science, Beijing Normal University, Beijing 100875, China.
E-mail address: caoxin@bnu.edu.cn (X. Cao).

https://doi.org/10.1016/j.agrformet.2020.108019
Received 15 August 2019; Received in revised form 16 April 2020; Accepted 25 April 2020
Available online 07 May 2020
0168-1923/ © 2020 Elsevier B.V. All rights reserved.

to climate change (Semenov, 2009; Xiao et al., 2015).

Traditionally, phenological information can be obtained through ground observation following predefined criteria (Boschetti et al., 2009; McMaster and Smika, 1998). Although the ground observation has the advantages of high precision and high time frequency, it is difficult to obtain the continuous phenological information in a large area due to its time-consuming and labor-intensive nature (Guo et al., 2016; Zhou et al., 2013). Remote sensing technology provides an alternative tool to investigate the spatial and temporal dynamics of phenology at regional or global scale (Chu et al., 2016; Cleland et al., 2007). Time-series of vegetation index (VI) data derived from satellite data from various sensors such as Advanced Very High Resolution Radiometer (AVHRR), Systeme Probatoire d'Observation de la Terre (SPOT) or MODerate-resolution Imaging Spectroradiometer (MODIS) have been widely used for phenology observation (Piao et al., 2006; Guyon et al., 2011; Zhang et al., 2003), among which Normalized Differential Vegetation Index (NDVI), Enhanced Vegetation Index (EVI) and two-band Enhanced Vegetation Index (EVI2) are commonly used (Beck et al., 2006; Qiu et al., 2017). However, it should be noted that each VI has its inherent shortcomings. When using different VI, it may bring uncertainty to the phenology detection results. For example, NDVI is liable to saturate in high leaf area index (LAI) (Carlson et al., 1990; Rama Rao et al., 2006), and is affected by soil background and bidirectional reflectance (Liu and Huete, 1995). EVI and EVI2 improve the performance in saturation and reduce the sensitivity to atmosphere and soil background (Thomsen et al., 2002), but they are still sensitive to topographic effect (Matsushita et.al, 2007). Besides, none of these VIs can effectively distinguish the VI increase caused by snow melting or vegetation growth in snow-covered areas, as snow melting may be confused with actual GUD (Wang et al., 2013; Shen et al., 2013). Recently, to address the issue, a new snow-free VI, i.e. Normalized Difference Phenology Index (NDPI) has been developed by Wang et al. (2017a) and demonstrated as a reliable VI for monitoring GUD in deciduous ecosystems, thanks to its insensitivity to snow and soil background (Chen et al., 2019). However, most of the existing studies applied these VIs to the phenology detection of natural ecosystems, and it is not clear how these VIs perform when detecting GUD of a crop ecosystem.

Currently, three types of methods have been employed to detect GUD from VI time series data, i.e. the thresholding method, the phenometrics derived from VI curve, and the curve match method (Zeng et al., 2020). The thresholding method determines GUD through a fixed VI threshold such as 0.099 (Lloyd, 1990) or a certain fraction of VI's amplitude (i.e., a relative threshold). The fixed threshold varies with vegetation types and environmental conditions, and it cannot be used in a large area universally (Chu et al., 2016). Thus, the fixed threshold is gradually replaced by the relative threshold. Commonly used relative thresholds are 10% (RT10) (Jönsson and Eklundh, 2002), 20% (RT20) (White et al., 1997) and 50% (RT50) (Sakamoto, 2018). The phenometrics-based method firstly fits the VI curve with a predefined mathematic function, e.g. the logistic function, and then defines GUD by reaching an inflection point, such as the maxima of the curvature change rate (CCR_{max}) (Zhang et al., 2003), and the maxima of the first derivation of the VI curve (β_{max}) (Lu et al., 2014). The curve match method firstly defines a shape model or a reference curve with given phenological dates. Then it matches the test VI curve with the predefined curve by model fitting, e.g. shape model fitting (SMF) (Sakamoto, 2018), or cross correlation, e.g. cross-correlogram spectral matching-phenology (CCSM-P) (Chen et al., 2016). Due to the variety of definitions and judgment rules of GUD in these detection methods, the choice of methods is another source of uncertainty in GUD detection (Liu et al., 2017). For example, some studies compared phenology detection results from the same datasets with various commonly-used methods and found significant differences, which could be up to ± 60 days (Schwartz et al., 2002; White et al., 2009; Vintrou et al., 2014). Moreover, the current GUD detection methods were initially proposed to study the phenology of forests or grasslands. On the other hand, the phenological characteristics of a crop system are more complex due to the multiple growth and rotation cycles under different agricultural practices (Wang et al., 2017b; Rama Rao et al., 2007). There is no consensus on which method is more suitable for crop system because such comparative studies are limited (Delbart et al., 2006; Lu et al., 2014; Wang et al., 2017a).

Considering the importance and uncertainty of detecting crop GUD by satellite data, we detected GUDs of winter wheat by using different combinations of four VIs and six methods in North China from 2009 to 2013, and evaluated the consistency of GUDs detected from VI data with ground-observed GUDs. The main objectives of this study were: (1) to find an appropriate VI and detection method to obtain more accurate GUD of winter wheat in the study area; (2) to explore the feasibility of applying a method over a large area by investigating the spatial trend of residuals from a linear model between satellite- and ground-observed GUDs. The results is expected to deepen the understanding of the interaction between crop systems and climate change.

2. Study area and data

2.1. Study area

The Huanghuai winter wheat region (108°24′−121°36′E, 29°01′−40°12′N), located in the North China Plain of P. R. China, was selected as the study area. It is the largest winter wheat planting region in China (Fig. 1). The study area consists of eight provinces (Hebei, Henan, Shanxi, Shandong, Shaanxi, Hubei, Anhui and Jiangsu) and two municipalities (Beijing and Tianjin). It is further divided into two sub-regions according to the characteristics of climate and wheat varieties (http://www.zys.moa.gov.cn/flfg/201904/t20190428_6245155.htm), namely the Huanghuai North (HHN) and the Huanghuai South (HHS). Under the temperate monsoon climate, the annual averaged temperature ranges from 17 °C to 5 °C from south to north, while the annual precipitation ranges from 2400 mm to 400 mm from southeast to northwest in this area. The dominant cropping system is a winter wheat and summer maize / rice rotation, with winter wheat cultivation from early October to mid-June of the following year and maize or rice from late June to late September (Sun et al., 2012). The winter wheat experiences two stages of growth, with the first growth in autumn and early winter before entering a dormancy period in winter, and the second from spring of the next year. The date the plant renews its growth and starts to grow rapidly is usually defined as the winter wheat GUD, which is mainly controlled by temperature accumulation (Wang et al., 2017b). With the spatial distribution of temperature, there is a similar spatial pattern of GUD in the whole region, which ranges from late February to late March from south to north.

2.2. Remote sensing and ground-observed data

The Moderate Resolution Imaging Spectroradiometer (MODIS) surface reflectance products (MOD09A1) with 500 m spatial resolution and 8-day temporal composite from 2009 to 2013 were used to calculate VI time series data. MOD09A1 data is a level-3 product and has been processed with geometric, radiometric and atmospheric corrections. Though maximum composition technique could reduce the noise effectively, there remain some disturbances in these VI time series caused by cloud contamination, atmospheric condition and bi-directional effects (Chen et al., 2004). Accordingly, an improved Savitzky-Golay filtering method (Cao et al., 2018) was used to smooth the original VI time series, further reducing the residual noise and ensuring that the VI time series can better show the growth process of winter wheat.

The winter wheat cropland map in 2013 was provided by Qiu et al. (2017). The spatial resolution of the map is 250 m with an overall accuracy of 88.86% (Qiu et al., 2017). Since the total planting area of winter wheat in the study area only changed less than 2% from

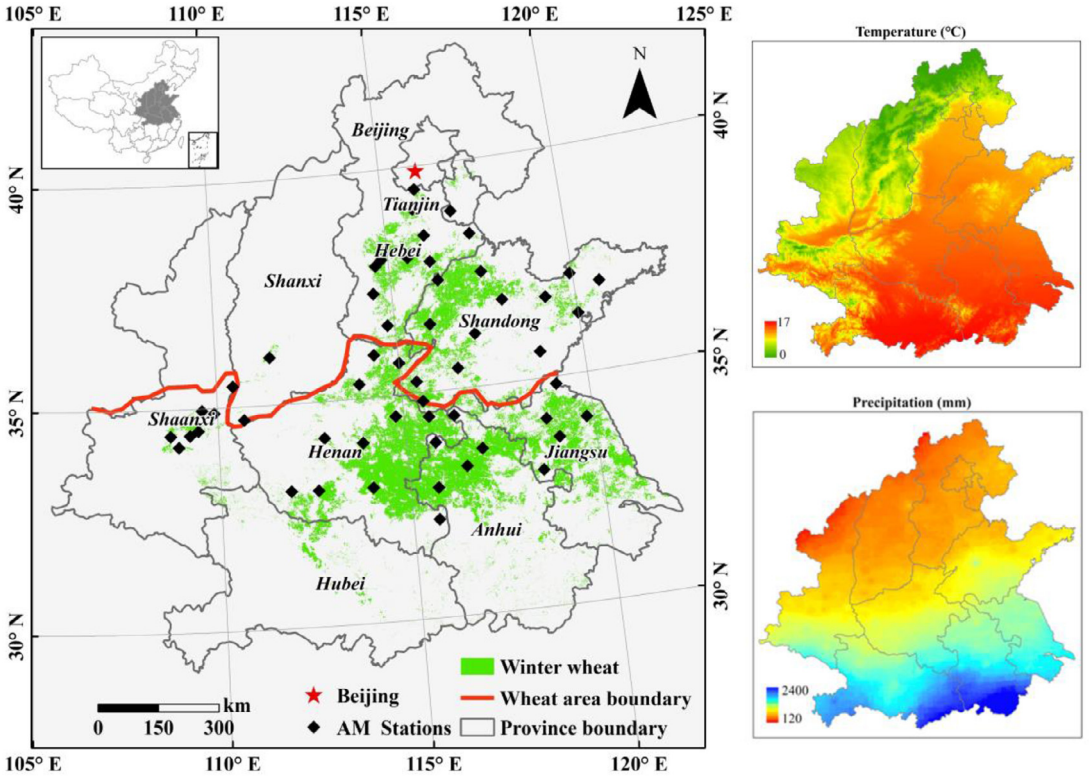

Fig. 1. The study area. The black diamonds are the agrometeorological (AM) stations, and the green regions are winter wheat planting areas provided by Qiu et al. (2017). The red line divides the whole study area into two winter wheat sub-regions, i.e. HHN and HHS. Right sub-figures are averaged patterns of multi-year mean temperature and total precipitation from 1981 to 2010 in the study area (Li et al., 2014). (For interpretation of the references to color in this figure legend, the reader is referred to the web version of this article.)

2009 to 2013 (http://www.stats.gov.cn), it can be reasonably assumed that the distribution of winter wheat is quite stable, eliminating the need for annual winter wheat maps.

Ground-observed GUD data for winter wheat during 2009–2013 were obtained from China Meteorological Data Sharing Service System (http://data.cma.cn/). The ground GUD was recorded by observers when half of the winter wheat leaves began to turn green and reached a length of 1–2 cm in a field near an agrometeorological station (Wang et al., 2017a). After excluding invalid records, 266 GUD records from 54 agrometeorological stations were finally used as the validation data.

3. Methodology

3.1. Vegetation indices

In this study, GUDs were identified on the time series of four MODIS-derived VIs, i.e. NDVI, EVI, EVI2 and NDPI. The calculations of the four VIs are listed in Table 1, where ρ_{red}, ρ_{NIR}, ρ_{blue} and ρ_{SWIR} are MODIS band 1, 2, 3 and 6, respectively.

3.2. GUD detection methods

In this study, we employed six different methods to detect GUDs of winter wheat, including RT10, RT20, RT50, β_{max}, CCR_{max} and CCSM-P. The descriptions of these methods are as follows.

For the relative thresholding method, GUD is defined as the date when VI value first reaches the 10% (RT10) or 20% (RT20) or 50% (RT50) of VI time series amplitude. VI time series amplitude is obtained by subtracting the minimum from maximum VI values in the annual VI cycle.

The CCR_{max} method (Zhang et al., 2003) uses a logistic function to fit a VI increasing period.

$$VI(t) = \frac{c}{1 + e^{a+bt}} + d \quad (1)$$

where t is the day of year; $VI(t)$ represents the VI value at time t; a, b, c and d are fitting parameters, of which a and b control the shape of VI growth curve, the sum of c and d is the maximum VI value, and d is the initial background VI value. Then GUD is identified as the timing with local maximum of curvature change rate, which is defined as:

Table 1
Vegetation indices used for winter wheat phenology detection and their calculations.

Vegetation index	Calculation	References
Normalized Difference Vegetation Index	$NDVI = \frac{\rho_{NIR} - \rho_{red}}{\rho_{NIR} + \rho_{red}}$	(Rouse et al., 1973)
Enhanced Vegetation Index	$EVI = 2.5 \times \frac{\rho_{NIR} - \rho_{red}}{\rho_{NIR} + 6 \times \rho_{red} - 7.5 \times \rho_{blue} + 1}$	(Liu and Huete, 1995)
Two-band EVI	$EVI2 = 2.5 \times \frac{\rho_{NIR} - \rho_{red}}{\rho_{NIR} + 2.4 \times \rho_{red} + 1}$	(Jiang et al., 2008)
Normalized Difference Phenology Index	$NDPI = \frac{\rho_{NIR} - \rho_{red}^{SWIR}}{\rho_{NIR} + \rho_{red}^{SWIR}}$ $\rho_{red}^{SWIR} = 0.74 \times \rho_{red} + 0.26 \times \rho_{SWIR}$	(Wang et al., 2017; Chen et al., 2019)

$$K' = b^3 cz \left\{ \frac{3z(1-z)(1+z)^3[2(1+z)^3 + b^2c^2z]}{[(1+z)^4 + (bcz)^2]^{\frac{5}{2}}} - \frac{(1+z)^2(1+2z-5z^2)}{[(1+z)^4 + (bcz)^2]^{\frac{3}{2}}} \right\} \quad (2)$$

where K' is the curvature change rate of the fitted VI curve, and $z = e^{a+bt}$.

The β_{max} method (Lu et al., 2014) is similar to CCR_{max} method except that the maximum slope is used to identify GUD. The slope of a logistic curve is defined as:

$$S = \frac{-bc}{(1+z)^2} \quad (3)$$

where S is the slope of the fitted VI curve, and $z = e^{a+bt}$.

The weighted cross-correlogram spectral matching-phenology (CCSM-P) was developed by Chen et al. (2016) to monitor interannual phenological changes by using the similarity between a target VI curve and a reference VI curve. The reference VI curve can be produced by averaging the VI curves of all years of interest, and the GUD of the reference curve is determined by CCR_{max} method or ground observation. The cross-correlogram matching is then performed by the following sequence: (1) shifting the target VI curve around GUD with a certain time interval, (2) calculating the matching degree between the shifted target VI curve and the reference VI curve, (3) defining the GUD of the target curve by the sum of GUD of the reference curve and the shifting days with the maximal matching degree. Chen et al. (2016) confirmed that CCSM-P showed robustness to noise and the capacity to capture the temporal trend of phenology. The matching degree $R_{w,m}$ between the target VI curve and the reference VI curve is calculated as below:

$$R_{w,m} = \frac{\sum_{i=1}^{n} w_i(\lambda_{t,i} - \bar{\lambda}_t^w)(\lambda_{r,i} - \bar{\lambda}_r^w)}{\sqrt{[\sum_{i=1}^{n} w_i(\lambda_{t,i} - \bar{\lambda}_t^w)^2][\sum_{i=1}^{n} w_i(\lambda_{r,i} - \bar{\lambda}_r^w)^2]}} \quad (4)$$

where m is the matching position, n is the number of overlapping days between VI reference and target VI curve, w_i is the weight of the i th matching point determined by the temporal distance to the GUD of reference curve, $\bar{\lambda}_t^w$ and $\bar{\lambda}_r^w$ are the weighted VI value averages of reference and target curve. Fig. 2 shows the schematic diagrams for GUDs detection by the six methods with NDPI curve.

3.3. Selection of pure winter wheat pixels

Due to the coarse spatial resolution of MODIS data, MODIS pixels may contain multiple land cover types. Mixed pixel effect will cause inconsistent GUD detection and bring uncertainty (Chen et al., 2018; Liu et al., 2019). In order to minimize the adverse impact of the mixed pixel effect, it is necessary to select 'pure' winter wheat pixels around each agrometeorological station from the winter wheat map.

When producing the winter wheat map, Qiu et al. (2017) proposed two indicators VE and VL, which were defined as the variations of VI curves during the early or late growth stages. The calculations of VE and VL are:

$$VE = (VI_{heading} - VI_{seedling}) + (VI_{max1} - VI_{min1}) \quad (5)$$

$$VL = (VI_{heading} - VI_{harvesting}) + (VI_{max2} - VI_{min2}) \quad (6)$$

where $VI_{seedling}$, $VI_{heading}$ and $VI_{harvesting}$ represent the VI values at estimated seedling, heading and harvesting dates of winter wheat; VI_{max1}, VI_{min1} represent the maximum, minimum VI values of winter wheat during the period from seedling date to heading date; and VI_{max2}, VI_{min2} represent the maximum, minimum VI values of winter wheat during the period from heading date to harvesting date. Since Qiu et al. (2017) found that VE and VL values of winter wheat were larger than those of other land covers, it can be reasonably assumed that a higher fraction of winter wheat in a pixel brings higher VE and VL values. Accordingly, VE and VL values of each pixel are used to select 'pure' winter wheat pixels. The steps are as follows: (1) selecting all pixels identified as winter wheat from the winter wheat map Qiu et al., 2017), and then calculating VE and VL values of the selected pixels for each year during 2009- 2013 by using four VIs (totally 40 values for each winter wheat pixel); ((2) Calculating mean and standard deviation values of these 40 values for each winter wheat pixel; (3) Selecting ten winter wheat pixels with the largest mean values within a 10 km distance around an agrometeorological station; (4) Selecting three pixels for each station with the smallest standard deviations from the ten winter wheat pixels. Through these steps, the selected winter wheat pixels were considered pure and unchanged from 2009 to 2013. Finally, we averaged the VI values of these three pixels, and took the GUD detected from this averaged VI time series as the satellite-observed result corresponding to the agrometeorological station.

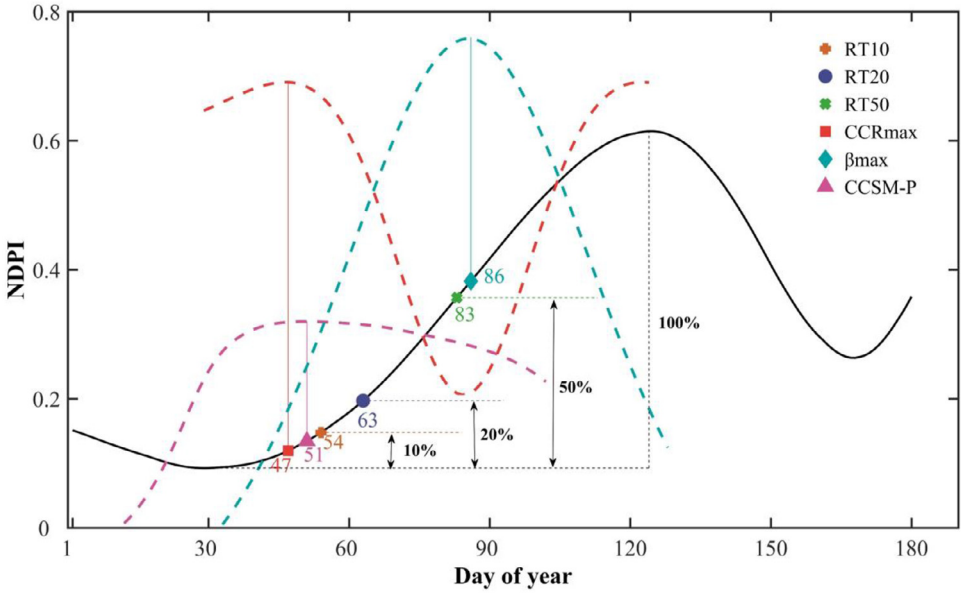

Fig. 2. The schematic diagram of the six methods detecting GUDs (the solid dots) with NDPI curve (the solid black line). Three relative thresholding methods are shown by the double arrows. The red dotted line is the curvature change rate of fitted logistic curve used in CCR_{max} method. The blue dotted line is the slope of the fitted logistic curve used in β_{max} method. The purple dotted line is the correlation coefficient between the shifted target NDPI curve and the reference NDPI curve used in CCSM-P method. (For interpretation of the references to color in this figure legend, the reader is referred to the web version of this article.)

3.4. Accuracy assessment and experiment design

The ground-observed GUD data from the agrometeorological stations was used to assess the accuracy or consistence of satellite-observed GUD results detected with aforementioned methods. Although ground and satellite observations differ in the definition of GUD, their trends had been proven to be consistent temporally and spatially (Guo et al., 2016). Thus, it is reasonable to assume that there is a linear relationship between the ground and the satellite observed GUD values. Therefore, we used a linear regression model, i.e. $y = ax + b$ to fit the ground- and satellite-observed GUDs, in which the ground-observed GUD is the independent variable and the satellite-observed GUD is the dependent variable. All satellite-observed GUDs from 2009 to 2013 were pooled together to be evaluated with the ground-observed GUDs. Four indicators were applied for accuracy evaluation, including the Pearson correlation coefficient (r), regression coefficient a, root mean square error (RMSE) and bias. Note that RMSE and bias were calculated with both satellite- and ground- observations before we applied the regression model.

We first used all GUDs to evaluate the performances of the four VIs in the whole region. Then we compared the accuracy of the six methods in HHN and HHS regions separately, combining with the VI that presented the best performance in the first step. Finally, we further analyzed the spatial coherence of the residuals from the above regression model to evaluate the spatial applicability of each method. Since temperature is the main control factor for GUD of winter wheat (Chu et al., 2016; Ding et al., 2016), and latitude is negatively correlated with temperature in the whole study area (Qiu et al., 2017), we used latitude as the proxy to represent the temperature and spatial characteristics.

4. Results

4.1. The performances of the VIs and methods

Using 5-year (2009–2013) ground-observed GUD data, we evaluated the performances of the VIs, i.e. NDVI, EVI, EVI2 and NDPI. Results show that all these four VIs combing with six methods can capture winter wheat GUD information to a certain extent with all r values greater than 0.4 (Fig. 3). Both NDPI and EVI achieve the highest mean value of r ($r_{mean} = 0.70$, $p < 0.01$) and standard deviation of r for NDPI is the lowest ($r_{std} = 0.02$), suggesting that NDPI has the best performance and robustness of all methods. On the other hand, NDVI presents the worst performance in detecting GUDs. Similarly, the regression parameter a referring to the slope of the fitted line also shows that NDPI outperforms the other three VIs with highest average of a values close to 1. The values of RMSE and bias are both less than 35 days, and there is no apparent difference in RMSE and bias for these four VIs. Considering the differences of GUD definition in six methods, comparison of RMSE and bias is not straightforward for performance evaluation of VIs. We thus only focused on the mean and standard deviation of r and a, from which GUDs detected by NDPI display a closer and more stable relationship with ground-observed GUDs than other three VIs.

The above results show that NDPI time series is the most suitable for GUDs detection. Accordingly, the performance of each method was further evaluated only by using NDPI time series in HHN and HHS regions (Fig. 4). In HHN region, GUDs detected with these six methods were significantly correlated with the ground observations with r values greater than 0.66. GUDs detected with RT50 method have the highest correlation r value with 0.74, while r value from RT10 method is the lowest with 0.66. But the difference between six r values is not significant. For RMSE and bias, GUDs detected with RT10, CCR_{max} and CCSM-P methods show the relatively smaller RMSE (~9 days) and bias (~2 day), while the RMSE and bias of GUDs detected with RT50 and β_{max} methods are much larger with values around 31 days and 30 days, respectively. And all six bias are greater than 0, indicating that all of these six methods overestimate GUDs to varying degrees in HHN region. As for the regression coefficient a, GUDs detected with CCR_{max} method show the highest degree of consistency with the ground-observed data with a value of 0.95, which is close to 1. However, in HHS region, the performances of all six models are poor with r values lower than 0.42. RT20 method instead of RT10 method presents the smallest RMSE (10.67 days). According to bias, RT20, RT50 and β_{max} methods overestimate GUDs while RT10, CCR_{max} and CCSM-P methods underestimate GUDs. Since RMSE mainly represents the proximity between the satellite and ground observations, RMSE is more suitable for accuracy evaluation. Accordingly, RT10, CCR_{max} and CCSM-P methods with relatively smaller RMSE values are recommended for GUD detection in HHN region, and RT20 method plays the same role in HHS region.

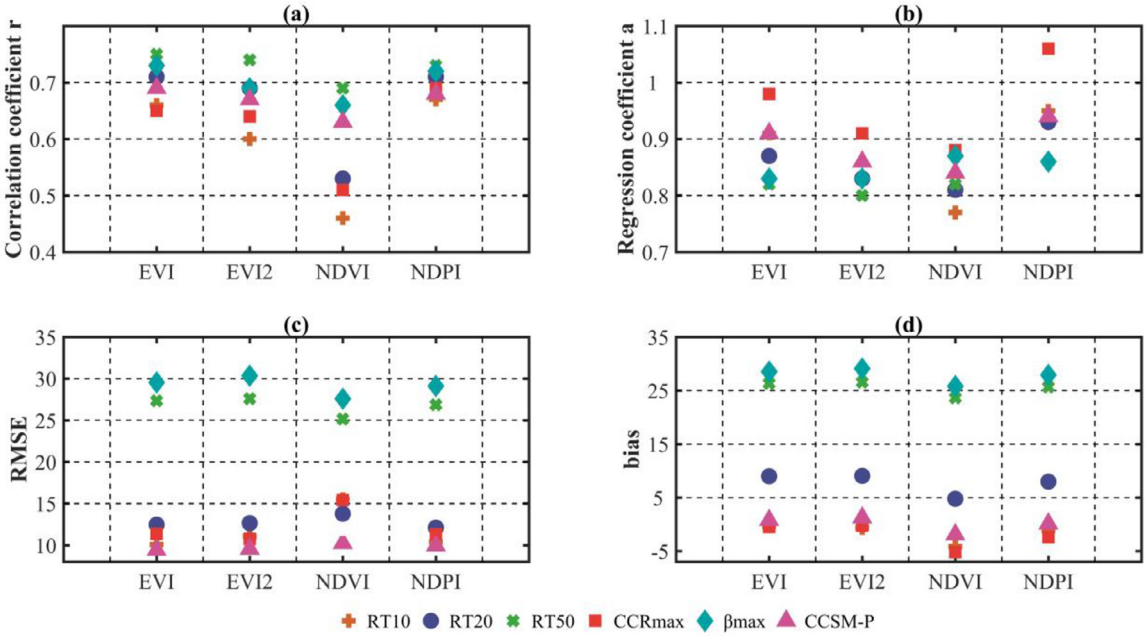

Fig. 3. Performance comparison of four VIs for GUD detection. Each VI cooperated with all six methods.

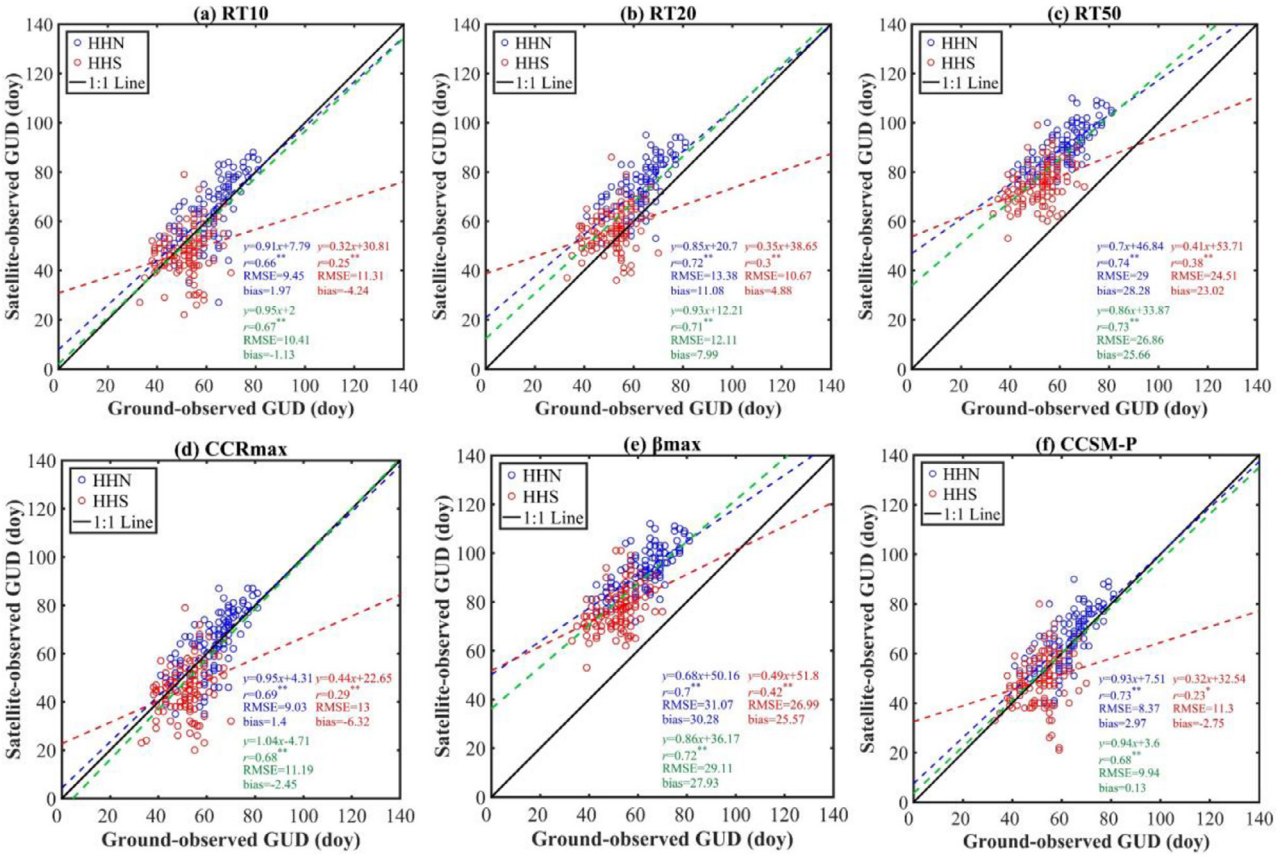

Fig. 4. Performance comparison of six GUD detection methods. The green dotted line represents the linear regression model fitted by all the data in the whole region. The symbol ** and * is significant at level of 0.01 and 0.05, respectively. (For interpretation of the references to color in this figure legend, the reader is referred to the web version of this article.)

4.2. Spatial feasibility of the GUD detection methods

In order to examine the spatial feasibility of the six methods, we further analyzed the relationship between the residuals from the six linear models in Fig. 4 and the latitude with a linear regression model, i.e. Residual = a latitude + b. The results are shown in Fig. 5. It is evident that all coefficients of determination (R^2) are significant at the level of 0.01 and all values of a are positive, indicating that there is a significantly positive correlation between residuals and latitudes for each method. RT10 method shows the highest a (2.65), suggesting the

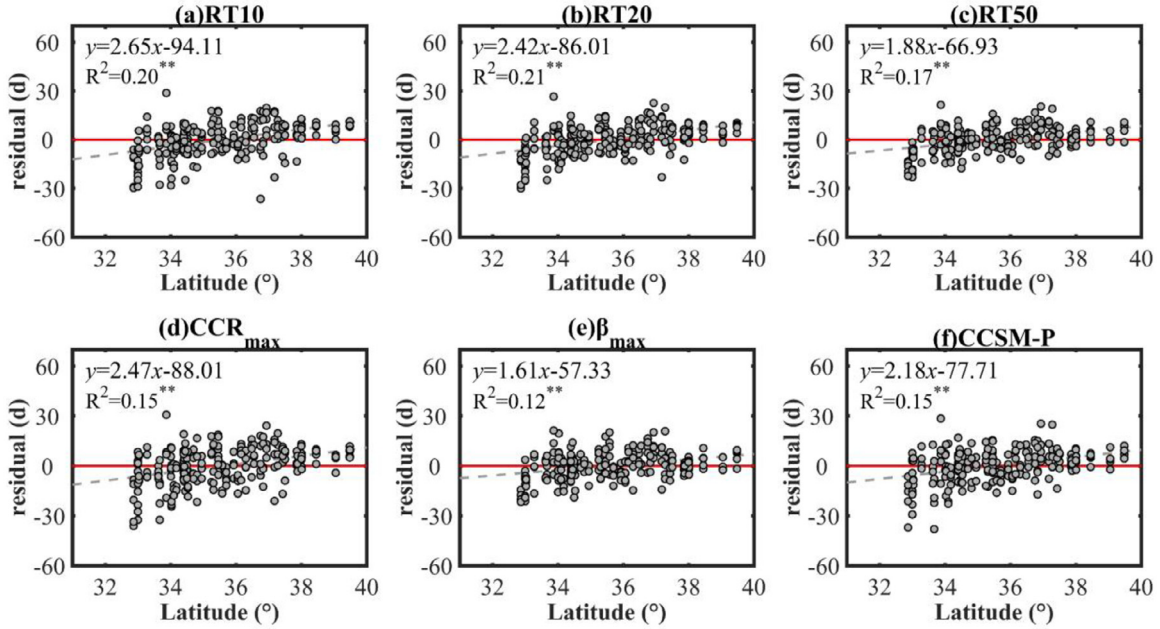

Fig. 5. The relationship between residuals from the six linear models in Fig. 4 and the latitude. The symbol ** means significance at level of 0.01.

strongest spatial coherence of residuals. The spatial trend of residuals from β_{max} method is the weakest with the lowest a (1.61) and R^2 (0.12) values. The results in Fig. 5 indicate that all methods fail to generate spatially consistent GUDs, with a tendency of underestimating (advancing) GUDs at low latitude regions and overestimating (delaying) GUDs at high latitude regions. The spatial coherence of residuals and latitude means that applying any of these six methods at a large-scale region might result in expanding the spatial variance of GUDs of winter wheat, which is not caused by the real GUD difference.

5. Discussion

5.1. The superiority of NDPI in GUD detection

In the study, we evaluated the performance of four commonly used VIs for GUD detection and found that GUDs from NDPI showed the best consistency with ground-based observations, followed by EVI and EVI2, while NDVI held the worst consistency. Similar studies have been carried out by other researchers. Peng et al. (2017) evaluated the accuracy of GUDs from MOD09Q1P_NDVI and MOD09Q1P_EVI over different vegetation types using ground GUD and AmeriFlux observation data. They found that GUDs detected from EVI time series overall had a better agreement with in situ observations than those from NDVI time series. The results are basically consistent with ours, because their study did not use NDPI. On the other hand, Huang et al. (2019) also compared the performances of NDVI and EVI in detecting GUD with trained optimal thresholds. They found no significant difference in accuracy between NDVI and EVI derived GUDs. This conclusion may be problematic, because their sample size was very small with data from only one year.

As is well known, during winter and early spring before GUD occurrence, the temperature condition is not favorable for winter wheat growth, resulting in a small canopy size and low coverage of winter wheat, and more bare soil mixed in a pixel scope. Moreover, the study region covers an extensive area with a large spatial heterogeneity in terms of climatic conditions and soil types. Higher soil coverage and larger differences in the soil type, soil color, and soil moisture conditions induce substantial variability in the VIs even if the vegetation conditions are identical. Accordingly, the adverse impact of the soil background on the VIs is more significant during the period of GUD occurrence with sparse vegetation, especially for NDVI (Montandon and Small, 2008). Compared to NDVI, EVI was proposed to alleviate the soil and atmospheric effects simultaneously based on the soil-line concept (Huete et al., 1994). However, different soil types correspond to different soil-lines, thus there is no single universal soil-line (Baret et al., 1993). Consequently, EVI based on soil-line conception may not completely reduce the soil effect across huge and heterogeneous areas. Different from the concept of the soil-line in EVI, NDPI uses a weighted red-SWIR (shortwave infrared) combination to replace the red band in NDVI, by which the value of combined red-SWIR band become almost equal to the value of NIR band for different types of soil. Therefore the values of NDPI for different types of soil approach to zero, while its sensitivity to the vegetation is unchanged (Wang et al., 2017b; Chen et al., 2019). Apart from significantly reducing the impact of soil background, NDPI is not susceptible to snowmelt. These two advantages could give NDPI a greater potential and superiority over the other VIs in monitoring GUD in large-scale regions.

5.2. Uncertainty of the six GUD detection methods

Existing studies have shown that some GUD detection methods can obtain similar results. For example, the percentage of VI curve amplitude at the GUD point detected by CCR_{max} method is constant at 9.18%, and at the GUD point detected by β_{max} method is 50% (Shang et al., 2017), that is, CCR_{max} is equivalent to RT10, and β_{max} is equivalent to RT50. Our results shown in Fig. 3 also support the conclusion that most of the GUDs detected by RT10 are close to CCR_{max}, while those detected by β_{max} are close to RT50. However, due to their respective inherent defects, these results are not completely consistent. The relative thresholding method is sensitive to the noises of VI curve, and its GUD detection results are easily affected by soil background, clouds and agricultural disasters. Different study areas or vegetation types need to find the appropriate thresholds. Huang et al. (2019) used ground phenology observations of all the agrometeorological stations in China to acquire the optimal relative thresholds for GUDs of different crops. And their results showed that the optimal relative thresholds for winter wheat, summer maize, spring maize and early rice are 9%, 1%, 31% and 30%, respectively. As for the phenometrics-based method, its performance of GUD detection depends on the fitting accuracy of VI curve, which is difficult to improve when VI curve does not follow the logistic curve (Cao et al., 2015). Moreover, this method could fail to detect GUD when VI value does not present abrupt increase at the time of GUD (Zeng et al., 2020). Finally, the CCSM-P method relies on the representativeness of the reference curve and the accuracy of the reference GUD detected from the reference curve. If there is considerable variability of VI curves among different years, the accuracy of GUD detection may be greatly affected (Zeng et al., 2020). Although RT10, CCR_{max} and CCSM-P methods are recommended for GUD detection in HHN region, as well as RT20 method for HHS region, more regional studies are needed to corroborate the robustness of these recommendations. Moreover, we remind users to pay more attention to the inherent defects and uncertainties of various methods when choosing GUD detection methods.

5.3. The causes of spatial dependency of the GUD detection methods

In the study, although the GUDs detected by the six methods have significant correlation with ground observations, their residuals are latitude dependent (Fig. 5), resulting in spatial unevenness of the fitting accuracy. We further explored whether the thresholds defined by ground-observed GUDs were related to latitude. We defined the percentage of NDPI curve amplitude at the ground-observed GUD point as the GGUD-threshold, and then established a linear model using the GGUD-threshold and latitude (Fig. 6a). As expected, GGUD-threshold also shows a significant negative correlation with latitude, which means that higher relative thresholds are required to detect GUDs for southern winter wheat. This is consistent with the conclusion in Fig. 4, which shows that RT10 method is suitable for GUD detection in HHN region, while RT20 is applicable in HHS region. There are two possible reasons for this latitude dependency. Firstly, the crop growth period after overwintering in south is shorter due to the larger development before overwintering. From the VI curves, southern winter wheat has higher VI values at the time of regrowth (Fig. 6b, blue dots and blue dash line), and the increment of VI values from the time of regrowth to the heading date are smaller (Fig. 6b, red dots and red dash line). Secondly, due to the large leaf area at the end of overwintering, the VI values of southern winter wheat increase significantly during the period of regrowth to GUD, as shown in Fig. 6c. Consequently, the relative increment of VI value at the time of GUD is greater for southern winter wheat than that for northern winter wheat. In other words, the lower the latitude, the higher the relative threshold for GUD detection. Accordingly, considering spatial dependency of the GUD detection methods, using different methods or thresholds over larger region may be a better choice to generate spatially consistent GUDs by VI data.

5.4. Mixed pixel effect on crop GUD dectection

Some studies have shown that the mixed pixel effect actually affects the accuracy of phenology detection based on VI data (Chen et al., 2018; Liu et al., 2019). Although the relatively pure winter wheat pixels were carefully selected to avoid the mixed pixel effect in this study, we cannot guarantee that these pixels are truly ‘pure’ ones due to the

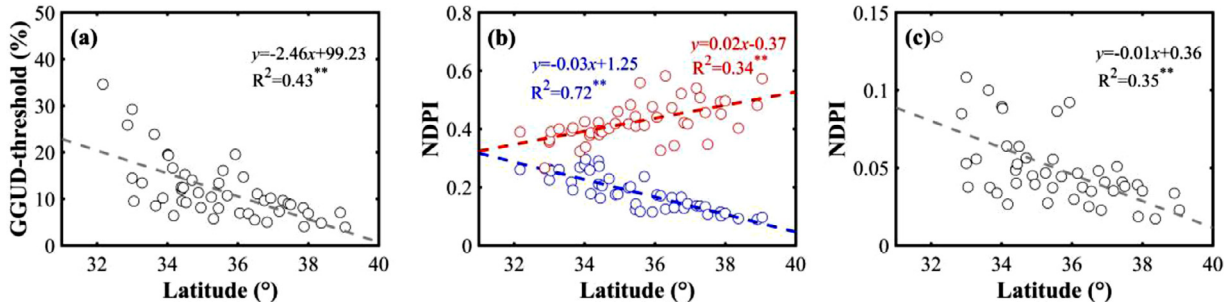

Fig. 6. (a) The relationship between GGUD-threshold (the percentage of NDPI curve amplitude at ground-observed GUD point) and latitude; (b) The relationship between the NDPI value increment from the time of regrowth in spring to the time when NDPI is at its maximum and latitude (red dots and red dash line), and the relationship between the NDPI value at the time of regrowth in spring and latitude (blue dots and blue dash line); (c) The relationship between the NDPI value increment from the time of regrowth in spring to the time of GUD and latitude; The symbol ** means significance at level of 0.01. (For interpretation of the references to color in this figure legend, the reader is referred to the web version of this article.)

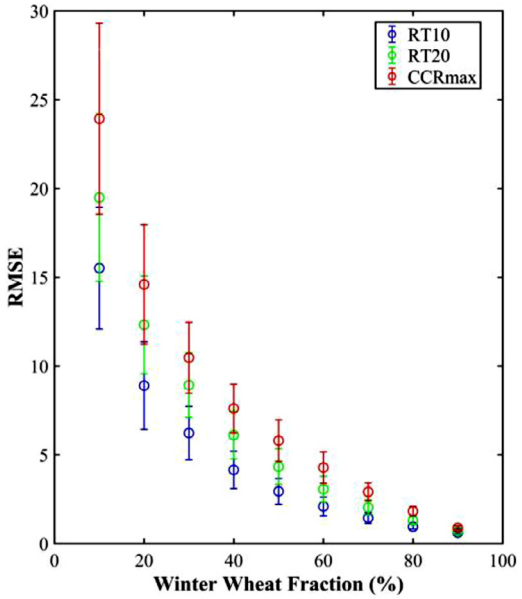

Fig. 7. The effect of the winter wheat fraction on the accuracy of GUD detection with RT10, RT20 and CCR_{max} methods from NDPI curves. The hollow dot is the average RMSE, and half the length of bar represents one standard deviation of RMSE.

coarse spatial resolution of MODIS data. To quantify the mixed pixel effect on satellite-observed GUDs, we carried out a simulation experiment. The NDPI curves of forest, grass, built-up, water and other cropland were selected, and NDPI curves of 'pure' winter wheat for each agrometeorological station were from Section 3.3. Then, a large number of the mixed pixels with coverages of 10% - 100% for winter wheat were generated by using a linear mixture model. Finally, using the RMSE indicator, GUDs detected from the simulated mixed pixels were evaluated with GUDs from the 'pure' winter wheat pixels (Fig. 7). When winter wheat coverage is greater than 60%, RMSE values approach stable with RMSE less than 5 days no matter which method is used. Considering that the temporal resolution of MODIS data is 8 days, the RMSE value caused by the mixed pixel effect would be acceptable. Accordingly, selecting the relatively pure pixels with coverage of winter wheat greater than 60% is sufficient to alleviate the impact of mixed pixels on the GUD detection accuracy based on NDPI data.

6. Conclusions

Using MODIS surface reflectance products with 8 day temporal resolution and 500 m spatial resolution during 2009–2013, this study comprehensively evaluated the performances of winter wheat green-up date (GUD) detection with four vegetation indices (NDVI, EVI, EVI2 and NDPI) combined with six methods (RT10, RT20, RT50, β_{max}, CCR_{max} and CCSM-P). Results show that satellite-derived GUDs significantly correlate with ground-observed data, and results based on NDPI present the highest accuracy and consistency, regardless of the methods used. Combined with NDPI, RT10, CCR_{max} and CCSM-P methods are more suitable to monitor GUD in the north of the study area (HHN region), while RT20 performs relatively well in the south of the study area (HHS region). We further investigated the residuals of detected GUDs with six methods and NDPI, and found that residuals of all methods showed a spatial trend, which might augment the spatial variance of GUDs. This finding indicated the spatial heterogeneity of the accuracy of these methods, which not only stresses the importance of appropriate methods for improving the accuracy of winter wheat GUDs detection using remote sensing data, but also presents a need for developing a new method or designing a new combination of existing methods to improve the spatial consistency of winter wheat GUDs at a large-scale region.

Declaration of Competing Interest

The authors declare that they have no known competing financial interests or personal relationships that could have appeared to influence the work reported in this paper

Acknowledgement

This research was funded by The National Key Research and Development Program of China (2017YFD0300201).

References

Badeck, F.-.W., Bondeau, A., Bottcher, K., Doktor, D., Lucht, W., Schaber, J., Sitch, S., 2004. Responses of spring phenology to climate change. New Phytol. 162, 295–309. https://doi.org/10.1111/j.1469-8137.2004.01059.x.

Baret, F., Jacquemoud, S., Hanocq, J.F., 1993. The soil line concept in remote sensing. Remote Sens. Rev. 7, 65–82. https://doi.org/10.1080/02757259309532166.

Beck, P.S.A., Atzberger, C., Høgda, K.A., Johansen, B., Skidmore, A.K., 2006. Improved monitoring of vegetation dynamics at very high latitudes: a new method using MODIS NDVI. Remote Sens. Environ. 100, 321–334. https://doi.org/10.1016/j.rse.2005.10.021.

Boschetti, M., Stroppiana, D., Brivio, P.A., Bocchi, S., 2009. Multi-year monitoring of rice crop phenology through time series analysis of MODIS images. Int. J. Remote Sens. 30, 4643–4662. https://doi.org/10.1080/01431160802632249.

Cao, R., Chen, Y., Shen, M., Chen, J., Zhou, J., Wang, C., Yang, W., 2018. A simple method to improve the quality of NDVI time-series data by integrating spatiotemporal information with the Savitzky-Golay filter. Remote Sens. Environ. 217, 244–257. https://doi.org/10.1016/j.rse.2018.08.022.

Cao, R., Chen, J., Shen, M., Tang, Y., 2015. An improved logistic method for detecting spring vegetation phenology in grasslands from MODIS EVI time-series data. Agric. For. Meteorol. 200, 9–20. https://doi.org/10.1016/j.agrformet.2014.09.009.

Carlson, T.N., Perry, E.M., Schmugge, T.J., 1990. Remote estimation of soil moisture

availability and fractional vegetation cover for agricultural fields. Agric. For. Meteorol. 52, 45–69. https://doi.org/10.1016/0168-1923(90)90100-K.
Chen, J., Jönsson, P., Tamura, M., Gu, Z., Matsushita, B., Eklundh, L., 2004. A simple method for reconstructing a high-quality NDVI time-series data set based on the Savitzky–Golay filter. Remote Sens. Environ. 91, 332–344. https://doi.org/10.1016/j.rse.2004.03.014.
Chen, J., Rao, Y., Shen, M., Wang, C., Zhou, Y., Ma, L., Tang, Y., Yang, X., 2016. A simple method for detecting phenological change from time series of vegetation index. IEEE Trans. Geosci. Remote Sens. 54, 3436–3449. https://doi.org/10.1109/TGRS.2016.2518167.
Chen, X., Guo, Z., Chen, J., Yang, W., Yao, Y., Zhang, C., Cui, X., Cao, X., 2019. Replacing the red band with the red-SWIR band (0.74ρred + 0.26ρswir) can reduce the sensitivity of vegetation indices to soil background. Remote Sens. 11, 851. https://doi.org/10.3390/rs11070851.
Chen, X., Wang, D., Chen, J., Wang, C., Shen, M., 2018. The mixed pixel effect in land surface phenology: a simulation study. Remote Sens. Environ. 211, 338–344. https://doi.org/10.1016/j.rse.2018.04.030.
Chu, L., Huang, C., Liu, Q.S., Liu, G.H., 2016. Estimation of winter wheat phenology under the influence of cumulative temperature and soil salinity in the Yellow River Delta, China, using MODIS time-series data. Int. J. Remote Sens. 37, 2211–2232. https://doi.org/10.1080/01431161.2015.1131871.
Cleland, E.E., Chuine, I., Menzel, A., Mooney, H.A., Schwartz, M.D., 2007. Shifting plant phenology in response to global change. Trends Ecol. Evol. 22, 357–365. https://doi.org/10.1016/j.tree.2007.04.003.
Delbart, N., Le Toan, T., Kergoat, L., Fedotova, V., 2006. Remote sensing of spring phenology in boreal regions: a free of snow-effect method using NOAA-AVHRR and SPOT-VGT data (1982–2004). Remote Sens. Environ. 101, 52–62. https://doi.org/10.1016/j.rse.2005.11.012.
Ding, D., Feng, H., Zhao, Y., Liu, W., Chen, H., He, J., 2016. Impact assessment of climate change and later-maturing cultivars on winter wheat growth and soil water deficit on the Loess Plateau of China. Clim. Change 138, 157–171. https://doi.org/10.1007/s10584-016-1714-1.
Estrella, N., Sparks, T.H., Menzel, A., 2007. Trends and temperature response in the phenology of crops in Germany. Glob. Change Biol. 13, 1737–1747. https://doi.org/10.1111/j.1365-2486.2007.01374.x.
Guo, L., An, N., Wang, K., 2016. Reconciling the discrepancy in ground- and satellite-observed trends in the spring phenology of winter wheat in China from 1993 to 2008. J. Geophys. Res. Atmos. 121, 1027–1042. https://doi.org/10.1002/2015JD023969.
Guyon, D., Guillot, M., Vitasse, Y., Cardot, H., Hagolle, O., Delzon, S., Wigneron, J.-.P., 2011. Monitoring elevation variations in leaf phenology of deciduous broadleaf forests from SPOT/VEGETATION time-series. Remote Sens. Environ. 115, 615–627. https://doi.org/10.1016/j.rse.2010.10.006.
Huang, X., Liu, J., Zhu, W., Atzberger, C., Liu, Q., 2019. The optimal threshold and vegetation index time series for retrieving crop phenology based on a modified dynamic threshold method. Remote Sens. 11, 1–22. https://doi.org/10.3390/rs11232725.
Huete, A., Justice, C., Liu, H., 1994. Development of vegetation and soil indices for MODIS-EOS. Remote Sens. Environ. 49, 224–234. https://doi.org/10.1016/0034-4257(94)90018-3.
Jiang, Z., Huete, A., Didan, K., Miura, T., 2008. Development of a two-band enhanced vegetation index without a blue band. Remote Sens. Environ. 112, 3833–3845. https://doi.org/10.1016/j.rse.2008.06.006.
Jonsson, P., Eklundh, L., 2002. Seasonality extraction by function fitting to time-series of satellite sensor data. IEEE Trans. Geosci. Remote Sens. 40, 1824–1832. https://doi.org/10.1109/TGRS.2002.802519.
Khare, S., Ghosh, S.K., Latifi, H., Vijay, S., Dahms, T., 2017. Seasonal-based analysis of vegetation response to environmental variables in the mountainous forests of Western Himalaya using Landsat 8 data. Int. J. Remote Sens. 38 (15), 4418–4442. https://doi.org/10.1080/01431161.2017.1320450.
Li, T., Zheng, X., Dai, Y., Yang, C., Chen, Z., Zhang, S., Wu, G., Wang, Z., Huang, C., Shen, Y., Liao, R., 2014. Mapping near-surface air temperature, pressure, relative humidity and wind speed over Mainland China with high spatiotemporal resolution. Adv. Atmos. Sci. 31, 1127–1135. https://doi.org/10.1007/s00376-014-3190-8.
Liu, H.Q., Huete, A., 1995. A feedback based modification of the NDVI to minimize canopy background and atmospheric noise. IEEE Trans. Geosci. Remote Sens. 33, 457–465. https://doi.org/10.1109/36.377946.
Liu, L., Cao, R., Shen, M., Chen, J., Wang, J., Zhang, X., 2019. How does scale effect influence spring vegetation phenology estimated from satellite-derived vegetation indexes? Remote Sens. 11. https://doi.org/10.3390/rs11182137.
Liu, Z., Wu, C., Liu, Y., Wang, X., Fang, B., Yuan, W., Ge, Q., 2017. Spring green-up date derived from GIMMS3g and SPOT-VGT NDVI of winter wheat cropland in the North China Plain. ISPRS J. Photogramm. Remote Sens. 130, 81–91. https://doi.org/10.1016/j.isprsjprs.2017.05.015.
Lloyd, D., 1990. A phenological classification of terrestrial vegetation cover using shortwave vegetation index imagery. Int. J. Remote Sens. 11, 2269–2279. https://doi.org/10.1080/01431169008955174.
Lu, L., Wang, C., Guo, H., Li, Q., 2014. Detecting winter wheat phenology with SPOT-VEGETATION data in the North China Plain. Geocarto Int. 29, 244–255. https://doi.org/10.1080/10106049.2012.760004.
Matsushita, B., Yang, W., Chen, J., Onda, Y., Qiu, G., 2007. Sensitivity of the Enhanced Vegetation Index (EVI) and Normalized Difference Vegetation Index (NDVI) to topographic effects: a case study in high-density cypress forest. Sensors 7, 2636–2651. https://doi.org/10.3390/s7112636.
McMaster, G.S., Smika, D.E., 1998. Estimation and evaluation of winter wheat phenology in the Central Great Plains. Agric. For. Meteorol. 43, 1–18. https://doi.org/10.1016/0168-1923(88)90002-0.
Montandon, L., Small, E., 2008. The impact of soil reflectance on the quantification of the green vegetation fraction from NDVI. Remote Sens. Environ. 112, 1835–1845. https://doi.org/10.1016/j.rse.2007.09.007.
Oteros, J., García-Mozo, H., Botey, R., Mestre, A., Galán, C., 2015. Variations in cereal crop phenology in Spain over the last twenty-six years (1986–2012). Clim. Change 130, 545–558. https://doi.org/10.1007/s10584-015-1363-9.
Peng, D., Wu, C., Li, C., Zhang, X., Liu, Z., Ye, H., Luo, S., Liu, X., Hu, Y., Fang, B., 2017. Spring green-up phenology products derived from MODIS NDVI and EVI: intercomparison, interpretation and validation using National Phenology Network and AmeriFlux observations. Ecol. Indic. 77, 323–336. https://doi.org/10.1016/j.ecolind.2017.02.024.
Piao, S., Fang, J., Zhou, L., Ciais, P., Zhu, B., 2006. Variations in satellite-derived phenology in China's temperate vegetation. Glob. Change Biol. 12, 672–685. https://doi.org/10.1111/j.1365-2486.2006.01123.x.
Qiu, B., Luo, Y., Tang, Z., Chen, C., Lu, D., Huang, H., Chen, Y., Chen, N., Xu, W., 2017. Winter wheat mapping combining variations before and after estimated heading dates. ISPRS J. Photogramm. Remote Sens. 123, 35–46. https://doi.org/10.1016/j.isprsjprs.2016.09.016.
Rama Rao, N., Garg, P.K., Ghosh, S.K., 2006. Estimation and comparison of Leaf Area Index of agricultural crops using IRS LISS-III and EO-1 Hyperion images. J. Indian Soc. Remote Sens. 34, 69–78. https://doi.org/10.1007/BF02990748. 1.
Rama Rao, N., Garg, P.K., Ghosh, S.K., 2007. Development of an agricultural crops spectral library and classification of crops at cultivar level using hyperspectral data. Precis. Agric. 8, 173–185. https://doi.org/10.1007/s11119-007-9037-x.
Richardson, A.D., Bailey, A.S., Denny, E.G., Martin, C.W., O'Keefe, J., 2006. Phenology of a northern hardwood forest canopy. Glob. Change Biol. 12, 1174–1188. https://doi.org/10.1111/j.1365-2486.2006.01164.x.
Rouse Jr., J., Haas, R.H., Schell, J.A., Deering, D.W., 1973. Monitoring Vegetation Systems in the Great Plains With ERTS. Third ERTS Symposium, pp. 309–317 NASA SP-351. 1.
Sakamoto, T., 2018. Refined shape model fitting methods for detecting various types of phenological information on major U.S. crops. ISPRS J. Photogramm. Remote Sens. 138, 176–192. https://doi.org/10.1016/j.isprsjprs.2018.02.011.
Schwartz, M.D., Reed, B.C., White, M.A., 2002. Assessing satellite-derived start-of-season measures in the conterminous USA. Int. J. Climatol. 22, 1793–1805. https://doi.org/10.1002/joc.819.
Semenov, M.A., 2009. Impacts of climate change on wheat in England and Wales. J. R. Soc. Interface 6, 343–350. https://doi.org/10.1098/rsif.2008.0285.
Shang, R., Liu, R., Xu, M., Liu, Y., Zuo, L., Ge, Q., 2017. The relationship between threshold-based and inflexion-based approaches for extraction of land surface phenology. Remote Sens. Environ. 199, 167–170. https://doi.org/10.1016/j.rse.2017.07.020.
Shen, M., Sun, Z., Wang, S., Zhang, G., Kong, W., Chen, A., Piao, S., 2013. No evidence of continuously advanced green-up dates in the Tibetan Plateau over the last decade. Proc. Natl. Acad. Sci. 110https://doi.org/10.1073/pnas.1304625110. E2329–E2329.
Sun, H., Xu, A., Lin, H., Zhang, L., Mei, Y., 2012. Winter wheat mapping using temporal signatures of MODIS vegetation index data. Int. J. Remote Sens. 33, 5026–5042. https://doi.org/10.1080/01431161.2012.657366.
Thomsen, A., Broge, N., Boegh, E., Schelde, K., Soegaard, H., Jensen, N.O., Hasager, C.B., 2002. Airborne multispectral data for quantifying leaf area index, nitrogen concentration, and photosynthetic efficiency in agriculture. Remote Sens. Environ. 81, 179–193. https://doi.org/10.1016/s0034-4257(01)00342-x.
Vintrou, E., Bégué, A., Baron, C., Saad, A., Seen, D.Lo, Traoré, S.B., 2014. A comparative study on satellite- and model-based crop phenology in West Africa. Remote Sens. 6, 1367–1389. https://doi.org/10.3390/rs6021367.
Wang, C., Chen, J., Wu, J., Tang, Y., Shi, P., Black, T.A., Zhu, K., 2017a. A snow-free vegetation index for improved monitoring of vegetation spring green-up date in deciduous ecosystems. Remote Sens. Environ. 196, 1–12. https://doi.org/10.1016/j.rse.2017.04.031.
Wang, S., Mo, X., Liu, Z., Baig, M.H.A., Chi, W., 2017b. Understanding long-term (1982–2013) patterns and trends in winter wheat spring green-up date over the North China Plain. Int. J. Appl. Earth Obs. Geoinf. 57, 235–244. https://doi.org/10.1016/j.jag.2017.01.008.
Wang, T., Peng, S., Lin, X., Chang, J., 2013. Declining snow cover may affect spring phenological trend on the Tibetan Plateau. Proc. Natl. Acad. Sci. 110, E2854–E2855. https://doi.org/10.1073/pnas.1306157110.
White, M.A., de Beurs, K.M., Didan, K., Inouye, D.W., Richardson, A.D., Jensen, O.P., O'Keefe, J., Zhang, G., Nemani, R.R., van Leeuwen, W.J.D., Brown, J.F., de Wit, A., Schaepman, M., Lin, X., Dettinger, M., Bailey, A.S., Kimball, J., Schwartz, M.D., Baldocchi, D.D., Lee, J.T., Lauenroth, W.K., 2009. Intercomparison, interpretation, and assessment of spring phenology in North America estimated from remote sensing for 1982-2006. Glob. Change Biol. 15, 2335–2359. https://doi.org/10.1111/j.1365-2486.2009.01910.x.
White, M.A., Thornton, P.E., Running, S.W., 1997. A continental phenology model for monitoring vegetation responses to interannual climatic variability. Glob. Biogeochem. Cycles 11, 217–234. https://doi.org/10.1029/97GB00330.
Xiao, D., Moiwo, J.P., Tao, F., Yang, Y., Shen, Y., Xu, Q., Liu, J., Zhang, H., Liu, F., 2015. Spatiotemporal variability of winter wheat phenology in response to weather and climate variability in China. Mitig. Adapt. Strateg. Glob. Change 20, 1191–1202. https://doi.org/10.1007/s11027-013-9531-6.
Zeng, L., Wardlow, B.D., Xiang, D., Hu, S., Li, D., 2020. A review of vegetation phenological metrics extraction using time-series, multispectral satellite data. Remote Sens. Environ. 237https://doi.org/10.1016/j.rse.2019.111511. 111511.
Zhang, X., Friedl, M.A., Schaaf, C.B., Strahler, A.H., Hodges, J.C.F., Gao, F., Reed, B.C., Huete, A., 2003. Monitoring vegetation phenology using MODIS. Remote Sens. Environ. 84, 471–475. https://doi.org/10.1016/S0034-4257(02)00135-9.
Zhou, L., He, H.L., Sun, X.M., Zhang, L., Yu, G.R., Ren, X.L., Wang, J.Y., Zhao, F.H., 2013. Modeling winter wheat phenology and carbon dioxide fluxes at the ecosystem scale based on digital photography and eddy covariance data. Ecol. Inform. 18, 69–78. https://doi.org/10.1016/j.ecoinf.2013.05.003.